nature communications

Article

https://doi.org/10.1038/s41467-026-71291-5

Light-induced bimerons in a chiral magnet

Received: 20 August 2025

Accepted: 18 March 2026

Published online: 01 April 2026

Check for updates

Kaixin Zhu[1,2], Filipp N. Rybakov[3], Zhan Wang[1,2], Wenli Gao[1,4], Shuaishuai Sun[1,5], Wentao Wang[1,2], Jun Li[1], Huanfang Tian[1], Olle Eriksson[3], Huaixin Yang[1,2], Ying Zhang[1,2,5], Nikolai S. Kiselev[6] ✉, Zian Li[7] ✉ & Jianqi Li[1,2,5] ✉

Controlled generation of topological spin textures, such as merons and their bound state, the bimerons, is essential for advancing spintronic technologies and elucidating soliton physics in condensed matter. Using in situ Lorentz transmission electron microscopy coupled with femtosecond laser pulse, we demonstrate the creation of two distinct Bloch-type bimeron states in chiral magnet $Co_8Zn_8Mn_4$ thin plates at room temperature. Magnetic imaging and micromagnetic simulations reveal that bimeron density varies with applied magnetic field strength, enabling dynamic topological control. We further establish that the topological classification of laser-generated bimerons is invariant with specimen thickness. Field-driven reversible transformations between elongated and circular bimeron morphologies are observed, governed by the competition of Zeeman energy and magnetic shape anisotropy. Micromagnetic simulations quantitatively reproduce these metastable states, validating a unified meron-skyrmion topological framework. This work establishes a single-pulse protocol for optical manipulation of topological spin textures.

Topological spin textures exhibit remarkable stability even at nanoscale dimensions, making them attractive for various non-volatile applications[1–4]. Their rapid response to external stimuli, such as electric currents, further positions them as promising candidates for information transfer elements in racetrack memory and quantum computing devices[5–8]. The prototypical two-dimensional topological magnetic solitons are skyrmions, which can be stabilized in magnetic systems with uniaxial magnetic anisotropy. In contrast, magnetic systems that exhibit easy-plane anisotropy host topological textures in the form of merons and related configurations. The stabilization of skyrmions generally results from a competition between Heisenberg exchange and other energy terms. For instance, in chiral magnets, the skyrmions are stabilized due to the Dzyaloshinskii-Moriya interaction (DMI) originating from a broken inversion symmetry of the crystal structure[9–11]. Besides that, skyrmions can also be stabilized by dipolar interactions[12], competing high-order interactions[13], and other factors[14]. Recent experimental studies have revealed a vast diversity of topological magnetic solitons, including high-order dipolar skyrmions[12,15], bimerons[16,17], skyrmion bags[18,19], and even hopfions[20–22] in the case of three-dimensional (3D) bulk samples.

Skyrmions in isotropic systems and systems with uniaxial anisotropy typically emerge within a magnetic background with collinear out-of-plane magnetization. The topology of such skyrmions is described in terms of the homotopy group $\pi_2(\mathbb{S}^2) = \mathbb{Z}$. The corresponding topological index, $Q \in \mathbb{Z}$ can be computed using the Kronecker integral[23]:

$$Q(\mathbf{m}) = \frac{1}{4\pi} \int_{\Omega} \mathbf{m} \cdot [\partial_{r_1} \mathbf{m} \times \partial_{r_2} \mathbf{m}] \, dr_1 dr_2, \tag{1}$$

where $\mathbf{m} \equiv \mathbf{m}(\mathbf{r})$ is the unit magnetization vector field, and Ω denotes the skyrmion localization region. This topological index is also widely

[1]Beijing National Laboratory for Condensed Matter Physics, Institute of Physics, Chinese Academy of Sciences, Beijing, China. [2]School of Physical Sciences, University of Chinese Academy of Sciences, Beijing, China. [3]Department of Physics and Astronomy, Uppsala University, Uppsala, Sweden. [4]School of Physics, Northwest University, Xi'an, China. [5]Songshan Lake Materials Laboratory, Dongguan, China. [6]Peter Grünberg Institute, Forschungszentrum Jülich, Jülich, Germany. [7]School of Physical Science and Technology, Guangxi University, Nanning, China. ✉e-mail: n.kiselev@fz-juelich.de; zianli@gxu.edu.cn; ljq@iphy.ac.cn

used to describe merons and their related configurations. However, it is important that Eq. (1) requires a very strict boundary condition – collinearity of spins at the perimeter of the integration domain, $\mathbf{m}(\mathbf{r} \in \partial\Omega) = \mathbf{m}_0$, for many real systems, such alignment around the textures of interest does not occur even approximately. Moreover, Eq. (1) is not invariant to the choice of coordinate system and can give values opposite in sign[20,24]. A theory of topological invariants for skyrmion-meron systems[25–28], which is free from the above-mentioned shortcomings, was presented in a recent work[29]. According to Ref. 29, the topological invariants of skyrmions and(or) merons must be described by a pair of integers (q_t, q_b), where $q_t = Q(\mathbf{m}_t)$ and $q_b = Q(\mathbf{m}_b)$ can be calculated with using Eq. (1). Here $\mathbf{m}_t$ and $\mathbf{m}_b$ denote the spin textures obtained via an auxiliary mapping of the magnetization and are referred to as the top and bottom projections, respectively. The principle of that auxiliary mapping and details of the topological charge calculation are provided in Supplementary Note 1. The corresponding homotopy group is isomorphic to the direct product of integers, which can be illustrated by the following relation[29]: $\pi_2(\mathbb{S}^2, \mathbb{S}^2 \backslash \{P_1, P_2\}) = \mathbb{Z} \times \mathbb{Z}$.

In idealized 2D chiral magnets with easy-plane anisotropy, merons can appear either as isolated objects (in a sense, that their cores can be isolated[29]) or in various bound configurations[25–28]. Due to topological and energetic constraints, they most often occur as coupled pairs, commonly referred to as vortex-antivortex pairs or bimerons[16,17]. Such bimerons have been theoretically predicted in a range of magnetic systems[30–33], and have been experimentally observed in epitaxial antiferromagnetic films[34], ferromagnetic multilayers[17], and thin plates of chiral magnets[16]. As particle-like spin textures, bimerons substantially have a promising potential for applications in electronics and spintronics[30–33,35,36]. Realizing controllable manipulation of bimerons is essential for advancing these applications[37,38].

Achieving controllable nucleation of topological spin textures is a crucial requirement for the practical application in spintronic devices. Light irradiation offers an ultrafast and versatile method for controlling the structural and magnetic properties of materials[39,40]. A femtosecond laser pulse can quench the long-range magnetic order on a picosecond timescale, producing a transient high-temperature state in which the magnetization undergoes abrupt local reversals, enabling skyrmion nucleation via localized spin dynamics[41,42]. On timescales from nanoseconds to microseconds, the dominant effect of the laser pulse is lattice heating. Even in this regime, relatively slow, thermally activated magnetization dynamics can still facilitate skyrmion nucleation[43]. The nucleation of vortex and antivortex in thin film with in-plane magnetization by means of femtosecond laser irradiation has also been reported[44–46]. However, the absence of particle-like behavior in isolated vortices and their random chirality make them less suitable for electronic and spintronic applications. The generation of bimerons in chiral magnets via femtosecond laser excitation has not yet been confirmed experimentally and is highly desirable for future applications.

In the following, we experimentally demonstrate that two distinct types of bimerons can be efficiently nucleated by laser pulses in a thin plate of $Co_8Zn_8Mn_4$ – a room temperature chiral magnet with isotropic (bulk type) DMI[47]. We further show that a relatively weak applied magnetic field can significantly shift the energy balance between them, favoring one type of bimeron over the other. We systematically investigated laser-generated bimeron clusters under various conditions, demonstrating that their density can be efficiently controlled by the strength of external out-of-plane magnetic field, and verifying that the topological classification of bimerons remains invariant across thin plates of differing thicknesses. Furthermore, we demonstrate the structural in-field evolution of bimerons, driven by the competition between the applied field and the shape anisotropy. These experimental findings are corroborated by micromagnetic simulations showing very good agreement with the experimental observations.

Results

Laser pulse-generated bimerons

In this work, we use a thin plate of $Co_8Zn_8Mn_4$ fabricated by the focused ion beam milling technique from a bulk crystal (see "Methods"). This compound belongs to a β-Mn-type Co-Zn-Mn alloys representing a unique type of chiral magnet with a Curie temperature above room temperature[47]. For instance, in our sample, we estimated the Curie temperature, $T_c \sim 350$ K, and the saturation magnetization at room temperature is $M_s \sim 240$ kA m^{-1} (Supplementary Fig. S2), which agrees with earlier studies[48,49]. In this study, all measurements were performed at room temperature.

We prepared a series of rectangular samples with thicknesses ranging from 90 to 200 nm. The characterization of the samples and a wide-field view of the samples are provided in Supplementary Figs. S3 and S5. In a thick $Co_8Zn_8Mn_4$ plate with thickness > 200 nm, the ground state is a helix with the **k**-vector lying in the sample plane. The equilibrium helix period was measured to be $L_D = 140$ nm. This value allows us to estimate the ratio between the Heisenberg exchange stiffness $\mathcal{A}$ and the DMI constant $\mathcal{D}$ using the well-established relation $L_D = 4\pi\mathcal{A}/\mathcal{D}$. In case of a plate with thickness much less than the smallest lateral dimensions of the sample $t \ll L$ ($L = \min(L_x, L_y)$), the effective easy-plane anisotropy can be approximated by the leading term of the demagnetizing field interaction, $K_s = \frac{1}{2}\mu_0 M_s^2$, as follows from the Γ-convergence limit[50–52]. In our case, the ratio $t/L \sim 0.02$ and such an approximation is meaningful. For the experimentally measured value of M_s, we estimated the constant of shape anisotropy for our sample as $K_s \approx 36$ kJ m^{-3}.

In agreement with experimental observations, the presence of easy-plane anisotropy changes the typical energy balance and favors the ground state of helix with **k**-vector pointing perpendicular to the plate (Supplementary Fig. S3). Due to the chiral surface twist effect[53–55], the system exhibits additional surface modulations which, in the case of a thin film, produce extra contrast in Lorentz transmission electron microscopy (TEM) images, most pronounced at low magnetic fields. These modulations are clearly visible in the experimental images in Supplementary Fig. S3, which show the ground state of the system for samples with thicknesses of 90, 140, and 200 nm.

Consistent with earlier studies, the micromagnetic model employed here accounts for the so-called FIB-damaged layer at the surfaces of our plates[18,20]. We approximate this layer as an 8 nm-thick region at both the top and bottom surfaces, where amorphization (loss of crystal symmetry) leaves the exchange stiffness and saturation magnetization nearly unchanged, but reduces the DMI to zero. This approximation proved essential for achieving quantitative agreement between theory and experiment. Supplementary Fig. S4 illustrates different behavior of the system in our simulations with and without a damaged layer.

To investigate the creation of room-temperature bimerons, we performed Lorentz TEM measurements on a $Co_8Zn_8Mn_4$ thin plate while exciting it with femtosecond laser pulses. The experimental setup is schematically illustrated in Fig. 1a. In a sample with a thickness of $t = 90$ nm ($\sim 0.65 L_D$), the initial magnetic configuration evolves into randomly distributed bimerons through an intermediate state that can be regarded as a pulsed laser induced disordered spin configuration (Fig. 1b). Four elementary merons that form bimerons are schematically depicted in Fig. 1c–f. Figure 1g, h shows representative spin textures of two types of bimerons along with the corresponding simulated Lorentz TEM images. The bimeron in Fig. 1g consists of a pair of merons topologically equivalent to those in Fig. 1c, d, whereas the bimeron in Fig. 1h consists of merons equivalent to those in Fig. 1e, f. These two spin textures correspond to topologically stable configurations. By contrast, bimerons composed of the merons in Fig. 1c, f, or in Fig. 1d, e, form topologically trivial configurations, since their indices satisfy (1, 0) + (−1, 0) = (0, 0) and (0, − 1) + (0, 1) = (0, 0), respectively. Such bimerons collapse immediately. Other combinations, such

https://doi.org/10.1038/s41467-026-71291-5

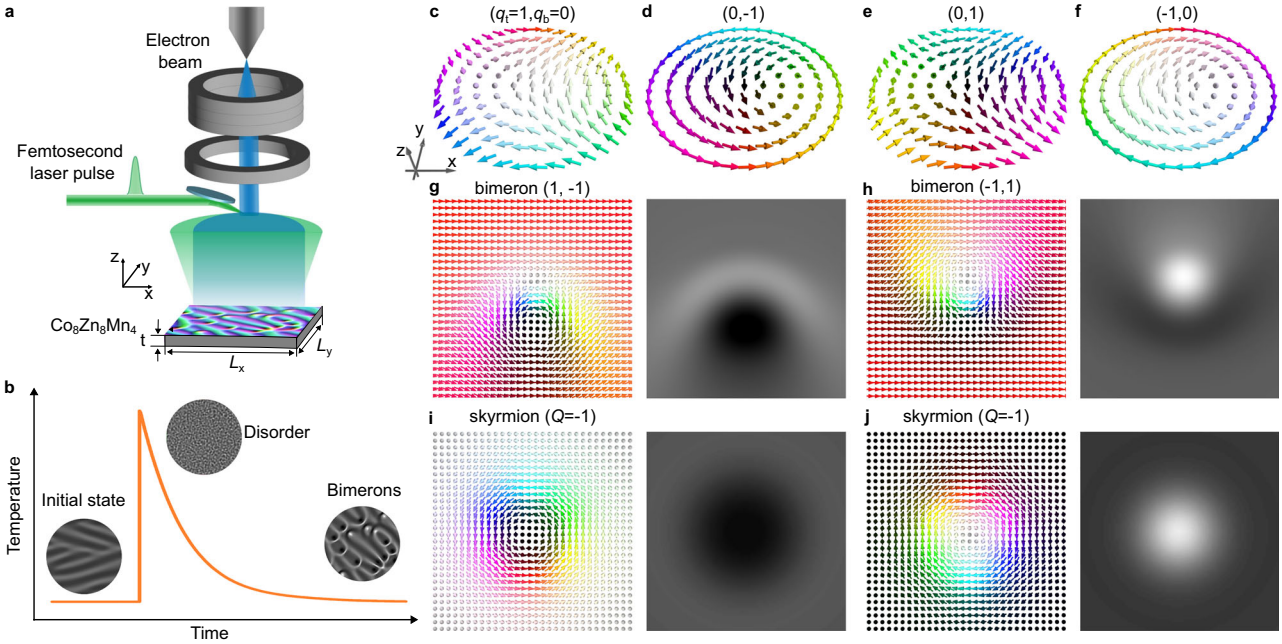

Fig. 1 | Individual merons and bimerons in a thin plate of a chiral magnet. **a** Schematic of experimental setup. The actual sizes of the electron beam and the laser beam spot are both larger than that of the sample. **b** Schematic of the fast demagnetization mediated bimeron nucleation process. The magnetic states evolve from the initial configuration via a disordered state to bimerons. **c**–**f** Four meron configurations, each characterized by a pair of topological indices (q_t, q_b) indicated in parentheses. The topological indices q_t and q_b correspond to Kronecker integral (1) calculated for top and bottom projections, respectively. Here and throughout the paper, we use the standard color code for magnetization vectors: white and black correspond to $m_z = 1$ and $m_z = -1$, respectively, while red, green, and blue indicate the azimuthal angle with respect to x axis. **g**. **h** Simulated textures of a ($q_t = 1, q_b = -1$) bimeron (**g**) and a ($q_t = -1, q_b = 1$) bimeron (**h**), and their corresponding theoretical under-focused Lorentz TEM contrast. **i**. **j** Simulated textures of elementary skyrmion observed/realized in two opposite polarizations, and corresponding theoretical under-focused Lorentz TEM contrast images.

as merons from Fig. 1c, e, or from Fig. 1d, f, are topologically stable but energetically unfavorable due to the isotropic DMI. Consequently, among the whole variety of possible bimerons, only the two bimerons shown in Fig. 1g, h remain both topologically and energetically stable.

With increasing perpendicular applied magnetic field or decreasing easy-plane anisotropy, the bimerons may undergo a transition into the pure skyrmions, as depicted in Fig. 1i, j. These two skyrmions can be superimposed onto each other and therefore differ only in polarity for the viewer. In terms of homotopy group analysis[29], the transition from (bi)merons to pure skyrmions can be described by the group homomorphisms $\mathbb{Z} \times \mathbb{Z} \to \mathbb{Z}$. Under such a transition, the topological indices of the merons shown in Fig. 1g and h transform according to the rules: $(q_t, q_b) \mapsto q_b$ and $(q_t, q_b) \mapsto q_t$, respectively. Contrary to the skyrmion configurations in Fig. 1i and j, which are characterized by axial symmetry, bimerons are asymmetric spin textures that emerge under the action of isotropic DMI. The (1, −1) bimeron consists of a crescent-shaped (1, 0) meron and a more circular (0,−1) meron. Similarly, the (−1, 1) bimeron is composed of a crescent-shaped (0, 1) meron and a circular (−1, 0) meron. As with the skyrmions in Fig. 1i, j, bimerons exhibit mutually inverted contrast in Lorentz TEM images, which allows one to distinguish them in experiment.

In all the studies presented below, we employ laser pulses with a duration of 300 fs and a fluence of 4.77 mJ cm^{-2} to irradiate the sample. To additionally examine the effect of laser parameters on bimeron generation, we systematically varied both the laser fluence and pulse width. Single-pulse excitations were applied with pulse durations of 200 fs, 800 fs, 2 ps, and 4 ps at different fluence levels. As shown in Supplementary Fig. S6, the laser fluences required for both bimeron generation and for reaching the maximum bimeron density do not exhibit a significant dependence on the laser pulse duration. From these data, we estimate the threshold laser fluence to be approximately 2 mJ cm^{-2}. Below this value, the magnetic texture does not exhibit noticeable changes after a single laser pulse. Since the beam's full width at half maximum (FWHM) is much larger than the sample size (see "Methods"), we can reasonably assume that the entire sample is homogeneously irradiated. A femtosecond laser pulse initially raises the sample temperature above the Curie temperature T_c, temporarily melting the long-range magnetic order[44,45]. The subsequent rapid cooling dissipates the system energy, bringing the sample temperature back below T_c. Simultaneously, the spin system begins to remagnetize, and the fast, non-equilibrium cooling generates numerous nanoscale spin clusters[56,57]. On a longer time scale, the system continues to lose energy to the environment, allowing the sample temperature to settle well below T_c. At this stage, these nanoscale spin clusters have sufficient time to interact, merge, and reorganize, ultimately coalescing into long-range, topologically non-trivial spin textures[56,57]. The details of the bimerons formation process are provided in Supplementary Note 3. Supplementary Video 1 shows an in-situ Lorentz TEM observation of a single laser pulse induced bimeron formation in a 30 mT perpendicular field, displaying the domain configuration before and after laser pulse excitation. A laser pulse rapidly excites the system, producing a post-pulse state independent of the initial configuration. As a result, consecutive pulses from low-repetition-rate lasers generate mutually independent states. This is evidenced by the observation that, at a fixed fluence, single-pulse excitations at repetition rates of 1, 10, and 100 Hz yield reproducible yet mutually independent bimeron configurations (Supplementary Fig. S8).

Finally, we emphasize that the threshold laser fluence of approximately 2 mJ cm^{-2} does not represent a sharply defined value. Instead, it spans a broad range between 1.75 and 2.3 mJ cm^{-2} (see Supplementary Fig. S6a, d). Therefore, the scenario in which laser excitation raises the sample temperature to just below, but close to, T_c cannot be excluded. As seen in Supplementary Fig. S6d, for laser fluences within this intermediate range, the initial magnetic configuration

https://doi.org/10.1038/s41467-026-71291-5

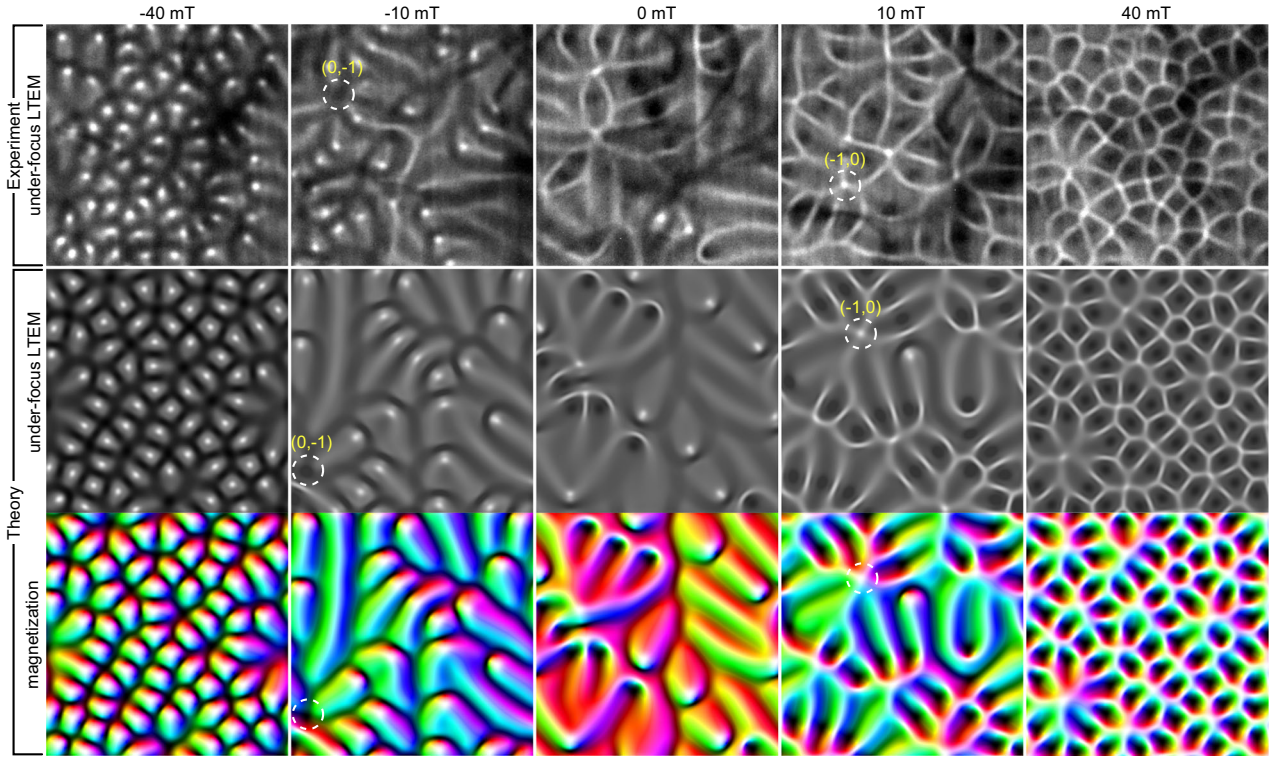

Fig. 2 | Topological spin textures induced by femtosecond laser pulses under different magnetic fields and corresponding micromagnetic simulations. The top row of images shows experimentally observed under-focus Lorentz TEM images of magnetic textures induced by femtosecond laser pulses at different magnetic fields applied perpendicular to the plate. The middle row of images shows theoretical under-focus Lorentz TEM contrast calculated for equilibrium magnetic texture obtained in micromagnetic simulations starting from a random spin distribution at the same applied magnetic field as in the experiment. The bottom row shows the corresponding magnetization vector field in the middle plane of the simulated sample. All of the experimental and theoretical images have identical sizes of 2 × 2 μm^2. The dashed circles in the images taken at −10 mT and 10 mT mark the positions of isolated merons with topological charges (0, −1) and (−1, 0), respectively.

may already be perturbed, allowing bimeron nucleation to occur. However, the highest bimeron densities are observed at substantially higher laser fluences. In this regime, the sample is most likely heated well above T_c, as indicated by the completely altered domain structure after every laser pulse (Supplementary Fig. S6d).

Control of bimeron density by external magnetic field

By applying current to the electron microscope objective lenses with an external current source, we can freely adjust the magnetic field applied perpendicular to the sample, and achieve free control of positive/zero/negative magnetic field. Figure 2 presents the response of a 90-nm-thick plate of $Co_8Zn_8Mn_4$ to femtosecond laser pulse excitations under positive/zero/negative magnetic fields. At zero magnetic field, bimeron with topological indices (1, −1) and (−1, 1) are energetically equivalent, and laser excitation generates both types of bimeron. However, even a relatively weak applied magnetic field can significantly alter the energy balance between them and favor bimerons of specific configurations. At small magnetic fields, such as 10 mT, the positive magnetic field reduces the energy of (1, −1) bimeron. This leads to more bimerons of this type to nucleate under laser pulse excitation. At low field, these bimerons are strongly disordered and accompanied by a small number of isolated (−1, 0) merons and (−1, 1) bimerons. Similar results can be obtained with laser excitation at an inverted magnetic field of −10 mT, with disordered (−1, 1) bimerons accompanied by a small number of (0, −1) merons and (1, −1) bimerons. Figure 2 also shows that at a relatively strong magnetic field of 40 mT, the laser pulses produce bimerons of only one type: (1, −1) bimerons in the case of positive field direction and (−1, 1) bimerons in the case of negative field direction.

It is worth noting that at low magnetic fields, where multiple bimerons coexist in close proximity, the distinction between individual bimerons becomes less well-defined. Since each bimeron consists of two merons, neighboring bimerons may share merons located in their vicinity. This overlap can lead to an apparent ambiguity in assigning a specific meron to a given bimeron. Nevertheless, the overall topological charge of the magnetic texture is determined by the total number of merons and antimerons. At higher magnetic fields, as shown below, this ambiguity disappears, and individual bimerons become well separated and easy to identify.

To emphasize the critical role of laser excitation in the nucleation of bimerons in our samples, we performed in-situ field cooling experiments on the samples. The samples were cooled from both the vicinity of the Curie temperature and temperatures well above it to room temperature under varying magnetic fields. In all field-cooling runs, no bimerons or other topological spin textures were observed. Instead, the system consistently relaxed into the global energy minimum state, i.e., the conical state. (Supplementary Fig. S9). This observation suggests that laser excitation is the direct cause of bimeron formation as an excited (metastable) state.

To investigate the magnetic structures arising from femtosecond laser pulse excitation, we conducted micromagnetic simulations where the initial state was set to a random spin distribution. These simulations were based on direct energy minimization and thereby represent a pseudo-dynamics. The resulting configurations are of primary importance, whereas the associated pathway may still offer qualitative insight without claiming to capture the true dynamics. The simulated domain has dimensions 2 μm × 2 μm × 90 nm with periodic boundary conditions applied in the *xy*-plane. Supplementary Fig. S7

https://doi.org/10.1038/s41467-026-71291-5

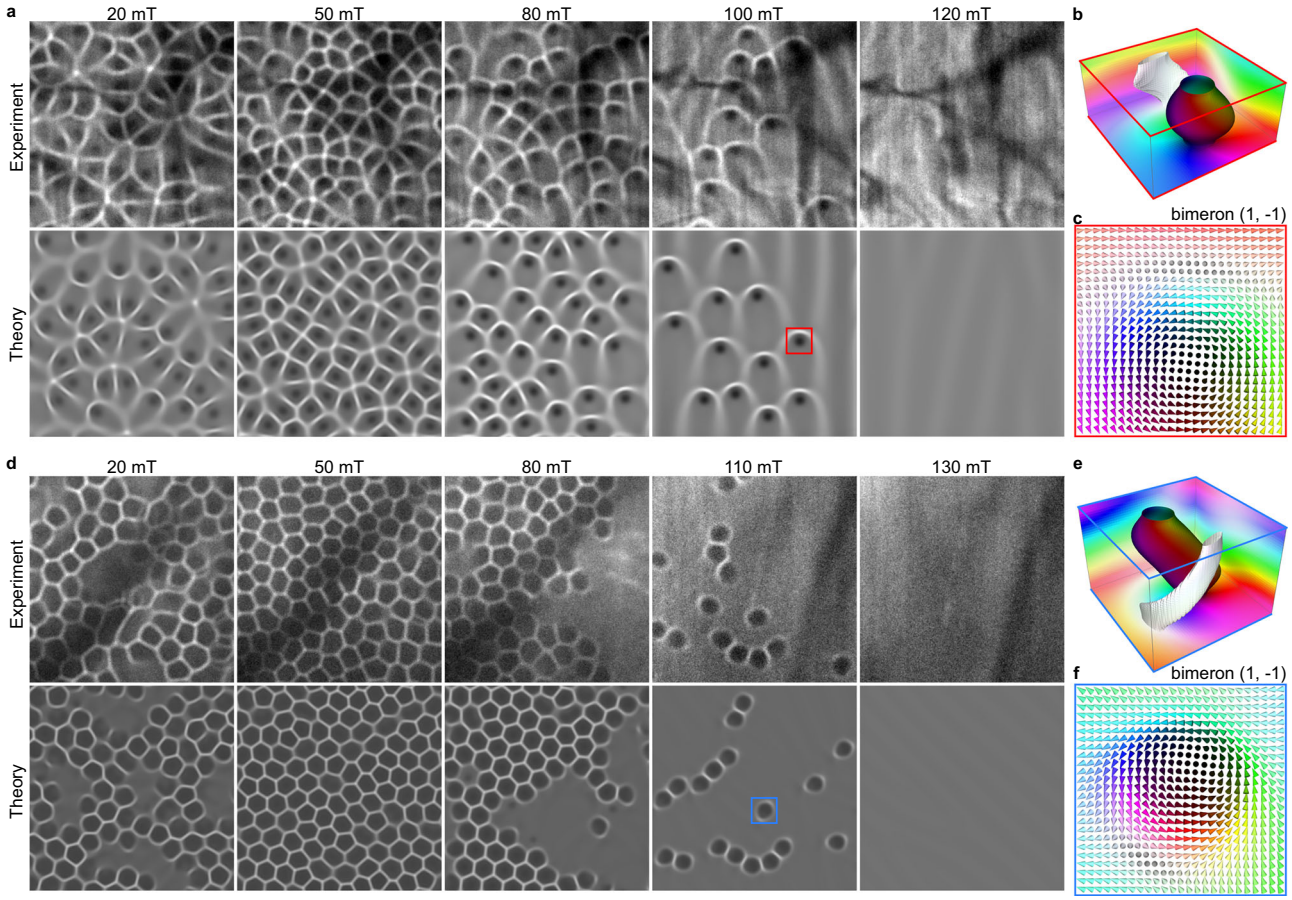

Fig. 3 | Comparison of laser-induced bimerons under varying magnetic fields in thin and thick plates. a Top: representative experimental Lorentz TEM images of laser-induced bimerons in a 90-nm-thick plate. Bottom: corresponding theoretical images from the simulations performed under the same applied field and bimeron density. **b** Magnetization vector field in the 200 × 200 × 90 nm^3 red square box marked in (**a**). The color code indicates the magnetic texture at the box edges, with two isosurfaces shown for $m_z = -0.5$ and $m_z = 0.95$. **c** Magnetization vector field in the mid-plane of the box shown in (**b**). **d** Same as (**a**), but for the 140-nm-thick sample. **e** Magnetization vector field in the 200 × 200 × 140 nm^3 blue square box marked in (**d**). **f** Mid-plane cross section of the magnetization in the box shown in (**e**). All of the experimental and theoretical images have identical sizes of 2 × 2 μm^2.

illustrates the evolution of the system and the corresponding theoretical Lorentz TEM contrast as the simulation approaches the equilibrium configuration corresponding to a specific local energy minimum. At the very beginning of the simulations, the system undergoes the scattering, nucleation, and annihilation of spin waves. Such a chaotic process gives rise to the nucleation of large, more ordered, and less quickly moving spin textures that relax into stable bimerons with well-defined configurations (Supplementary Fig. S7). Supplementary Video 2 illustrates this dynamic evolution process under zero magnetic field, which can be considered a rough approximation of the actual laser excitation process. Figure 2 displays snapshots of simulated final stable bimerons under varying magnetic fields after complete minimization of the micromagnetic energy, along with corresponding simulated Lorentz TEM images. These simulations demonstrate excellent agreement with experimental Lorentz TEM data.

Thickness effect

Figure 3 compares the laser-induced magnetic textures in samples with thicknesses of 90 and 140 nm under identical laser pulses. An extended series of images showing the nucleation of laser-induced bimerons under various positive and negative magnetic fields is provided in Supplementary Figs. S10–S13. With increasing applied magnetic field, the density of magnetic textures first rises to a maximum and then gradually decreases. Remarkably, the bimeron density in both thick and thin samples follows nearly the same field dependence. In both cases, the maximum density occurs at approximately 55 ± 5 mT. The threshold field above which laser pulses no longer nucleate new magnetic textures is about 125 ± 5 mT for both thicknesses.

Despite their nearly identical bimeron densities, samples of different thicknesses exhibit distinctly different Lorentz TEM contrasts for individual bimerons. In the thin film, each dark spot is bordered on one side by a bright, crescent-shaped halo. In the thick sample, the contrast is more symmetric, with the dark spot surrounded by an almost perfect bright ring. This might suggest that the texture in the thick film represents a skyrmion similar to those shown in Fig. 1i, j. Such interpretations are also frequently encountered in the literature[10,11]. Micromagnetic simulations, however, reveal that in both cases the underlying spin textures should be classified as bimerons.

The bottom row of images in Fig. 3a, d shows the theoretical Lorentz TEM contrast calculated for equilibrium spin configurations obtained by minimizing the micromagnetic energy functional. In these simulations, the bimeron density for each value of the external magnetic field was adjusted to visually match the experimental images. The resulting configurations reproduce the experimental contrasts with high fidelity, confirming the correspondence between the observed magnetic textures and those obtained in simulations.

To examine the magnetic texture in more detail, we select relatively isolated objects marked by red and blue squares in the thin and thick samples, respectively. Figure 3b and c show the magnetization configuration of a bimeron in a thin 90-nm film, while Fig. 3e, f display the corresponding configuration in a thick 140-nm sample. A clear

https://doi.org/10.1038/s41467-026-71291-5

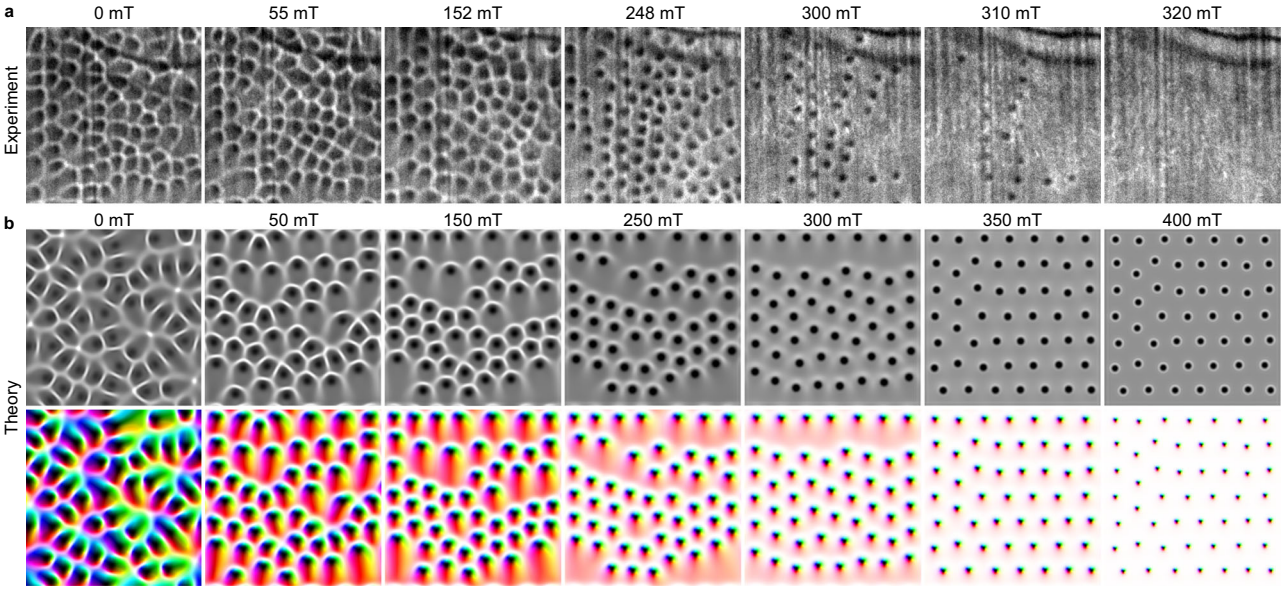

Fig. 4 | Magnetic field-controlled structural evolution of bimerons. a The observed evolution of the bimeron structure driven by the increased magnetic field in the experiment. **b** Micromagnetic simulation of bimeron-to-skyrmion transition under increasing fields in a 90-nm-thick sample, visualized via theoretical under-focus Lorentz TEM contrast and corresponding magnetization vector field. All of the experimental and theoretical images have identical sizes of 2 × 2 μm².

similarity is observed between the mid-plane magnetic textures in Fig. 3c, f: in both cases, the same (1, −1) bimeron appears, with the only difference being the relative positions of the meron cores. The isosurfaces of the bimerons in the thin and thick samples, shown in Fig. 3b, e, also reveal this similarity. The white isosurface corresponds to the core of the (1, 0) meron, while the colored isosurface surrounds the (0, −1) meron. The main difference between Fig. 3b, e is that, in the thick sample, the white isosurface winds around the colored one. As a result, the magnetization averaged over the thickness and projected into the plane perpendicular to the electron beam exhibits partial blurring of the (1, 0) meron around the circular core of the (0, −1) meron. This produces a more axially symmetric, ring-like contrast in Lorentz TEM images for the thick film. In the thicker plate ($t > 1L_D$), the bimeron contrast appears more symmetric in Lorentz TEM, and is generally interpreted as a skyrmion tube surrounded by the cone phase[58–61]. However, in a thin plate ($t \leq 1L_D$), the surrounding cone phase is more meron-like, and it is appropriate to describe the topological texture as bimeron. Nevertheless, bimerons in thin and thick plates depicted in Fig. 3 remain topologically equivalent. The complete three-dimensional spin configurations corresponding to Fig. 3a (100 mT) and d (110 mT) are provided in the Source Data and can be used for alternative visualization of the magnetic textures shown in Fig. 3b, c, e, f.

Field-induced bimeron-skyrmion transition

The transitions between bimerons and skyrmions, illustrated in Fig. 1g, i (or Fig. 1h, j), can in principle be induced by increasing the external magnetic field above the critical value $B_c = 2(K_s + K_D)/M_s$, where $K_s = \frac{1}{2}\mu_0 M_s^2$ is the shape-anisotropy contribution and $K_D = \mathcal{D}^2/(4\mathcal{A})$ is the effective anisotropy induced by bulk DMI[61,62]. For $Co_8Zn_8Mn_4$, this critical field is estimated to be $B_c \approx 400$ mT. Above B_c, the cone phase surrounding the bimeron transforms into a saturated ferromagnetic state, and the bimeron texture undergoes a transition into a skyrmion regardless of sample thickness. To investigate this transition, we performed a systematic study of bimerons in a 90-nm-thick sample under an applied magnetic field. (1,−1) Bimerons were first generated by a laser pulse at a low positive magnetic field. The field was then reduced to zero, and an image was recorded. Subsequently, the applied magnetic field was gradually increased, and images of the magnetic states were captured at various field strengths. The row of images in Fig. 4a presents experimental Lorentz TEM images obtained in a 90-nm-thick sample over the field range 0–320 mT. With increasing field, the asymmetric contrast characteristic of an individual bimeron gradually evolves into a more symmetric shape. In the under-focused Lorentz TEM images, the dark spot becomes smaller, while the surrounding bright, crescent-shaped halo becomes less pronounced. In the range from 0 to 250 mT, the field-driven evolution of the bimerons is fully reversible (see Supplementary Fig. S15). Above 250 mT, the number of bimerons steadily decreases, and above 320 mT, they disappear completely.

The micromagnetic simulations shown in Fig. 4b exhibit good agreement with the experimental images. Similar to the experimental protocol, the simulations were initialized under an applied field of 30 mT starting with a random magnetization distribution, performed energy minimization, and then the field was reduced to zero. The main difference between the experimental and simulated results is that bimeron collapse is not observed at the same field values in the simulations. This discrepancy is typical for micromagnetic simulations that do not include temperature effects. On the other hand, the results of direct energy minimization are in good agreement with the stochastic LLG simulations within the micromagnetic model (Supplementary Fig. S16), even though finite-temperature effects cannot be fully captured in continuum descriptions.

In micromagnetic simulations, the bimerons remain stable up to, and even above, the critical field $B_c = 400$ mT. Thus, in the simulations, we observe a field-driven transition from bimerons to skyrmions. This transition is evident from the background magnetization color in the bottom row of Fig. 4b. At low field, the background has a reddish hue, indicating that in the mid-plane the surrounding magnetization has an in-plane component oriented along the x-axis. With increasing field, the background between bimerons becomes brighter, and at 400 mT it appears white, indicating that the bimerons have transformed into skyrmions embedded in a ferromagnetic background. In the experiment, however, all bimerons collapse at much lower fields, so strictly speaking, such a transition does not occur. Therefore, even though at high magnetic fields the experimentally observed contrast resembles

that of skyrmions (Fig. 4a), we classify these spin textures as bimerons embedded in a conical background. In fact, most of the spin textures reported as skyrmions in isotropic chiral magnets with bulk DMI should more accurately be classified as bimerons[58,59,61,63].

Discussion

In summary, we present a comprehensive protocol for generating two distinct bimeron types at room temperature in $Co_8Zn_8Mn_4$ thin plates using femtosecond laser pulses within TEM. Homotopy group analysis assigns topological invariants (1, −1) and (−1, 1) to these bimerons. We demonstrate that the density of laser-induced bimerons can be efficiently tuned through applied magnetic fields. Combining experiments and micromagnetic simulations, we verified the unified bimeron-skyrmion topological framework. Our micromagnetic model incorporates both demagnetizing field effects and fabrication-induced surface damage. Realistic simulations based on this model, alongside corresponding theoretical Lorentz TEM images, exhibit excellent quantitative agreement with experimental data. These simulations predict a high-field structural transition from bimeron to skyrmion, though thermal fluctuations at room temperature preclude experimental observation. Low-temperature studies of in-field bimeron evolution are proposed to enable direct observation of this transition. Collectively, these results establish the feasibility of optical writing of topological spin textures in in-plane magnetized thin films and provide a foundation for engineering novel topological states for spintronic applications.

Methods

Bulk sample preparations

Polycrystalline $Co_8Zn_8Mn_4$ samples were synthesized following the method described in ref. 47. Stoichiometric amounts of pure Co, Zn, and Mn pieces, with a total mass of 5 g, were sealed in evacuated quartz tubes (10^{-3} Pa) and heated to 1000 °C for 12 h. The samples were subsequently cooled slowly at a rate of 1 °C h^{-1} to 925 °C and maintained at this temperature for 75–100 h. Finally, the products were subjected to water quenching.

TEM sample preparation

$Co_8Zn_8Mn_4$ thin lamellae were fabricated from bulk crystals using a scanning electron microscopy-focused ion beam (SEM-FIB) dual-beam system (JIB-4700F Multi Beam System) equipped with a gas injection system and a micromanipulator. A lamella with an initial thickness of ~1 µm was extracted from the bulk crystal using the lift-out method, then transferred onto a copper lift-out grid via the deposited Pt layers. Depending on the experimental requirements, the samples were subsequently thinned to a final thickness of 90–200 nm. A low ion beam current was applied for final polishing to minimize the surface amorphous layer.

Magnetic imaging and femtosecond laser excitation

Fresnel-defocus Lorentz TEM was employed for magnetic domain analysis using a JEOL JEM-2100 Plus microscope operated at 200 kV. The objective lens current was precisely regulated to apply out-of-plane magnetic fields ranging from −1.0 T to +1.0 T normal to the specimen plane. All images were acquired at room temperature using a Gatan OneView 4k × 4k detector, with the defocus distance maintained at 1 mm unless otherwise specified. The JEM-2100 Plus microscope was retrofitted with a femtosecond laser system (Spirit 1040-4, Spectra-Physics), enabling direct generation of bimerons in $Co_8Zn_8Mn_4$ thin plates via pulsed laser excitation. Linearly polarized 520 nm femtosecond pulses (300 fs FWHM duration) were focused to a ~40 µm FWHM spot on the specimen. These pulses were generated by frequency-doubling the fundamental 1040 nm output in a β-barium borate (BBO) crystal, with pulse energy and repetition rate digitally controlled.

Micromagnetic simulations

In this work, we follow the micromagnetic model approach with the total energy of the system, including four energy terms: the Heisenberg exchange energy, DMI energy, Zeeman energy, and self-energy of the demagnetizing field:

$$\varepsilon = \int_{V_m} \mathrm{d}\mathbf{r}\, \mathcal{A} \sum_{i=x,y,z} |\nabla m_i|^2 + \mathcal{D}\,\mathbf{m}\cdot(\nabla\times\mathbf{m}) - M_s\,\mathbf{m}\cdot\mathbf{B} + \frac{1}{2\mu_0}\int_{\mathbb{R}^3}\mathrm{d}\mathbf{r} \sum_{i=x,y,z} |\nabla A_{d,i}|^2, \quad (2)$$

where $\mathbf{m}(\mathbf{r}) = \mathbf{M}(\mathbf{r})/M_s$ is a unit vector field that defines the direction of the magnetization, $M_s = |\mathbf{M}(\mathbf{r})|$ is the saturation magnetization, $\mathcal{A}$ is the exchange stiffness constant, $\mathcal{D}$ is the constant of isotropic bulk DMI, and μ_0 is the vacuum permeability. The magnetic field in Eq. (2), $\mathbf{B} = \mathbf{B}_{ext} + \nabla\times\mathbf{A}_d$, is the sum of the external magnetic field and the demagnetizing field, where $\mathbf{A}_d(\mathbf{r})$ is the component of the magnetic vector potential induced by the magnetization. In our simulations, we used the following material parameters for $Co_8Zn_8Mn_4$: $\mathcal{A} = 5.8$ pJ m^{-1}, $\mathcal{D} = 0.52$ mJ m^{-2}, and $M_s = 240$ kA m^{-1}. The value of M_s corresponds to room temperature, as shown in Supplementary Fig. S2. With these parameters, the equilibrium period of helical modulations at zero field is $L_D = 4\pi\mathcal{A}/\mathcal{D} = 140$ nm, in agreement with the experiment (see Supplementary Fig. S3). The saturation field of the conical phase[59] is given by $B_c = B_D + \mu_0 M_s \approx 400$ mT, where $B_D = \mathcal{D}^2/(2M_s\mathcal{A})$.

The simulation domain was set to 2×2 µm^2 in the xy-plane, with the thickness varied between 90 and 200 nm. The discretization size in the finite-difference scheme was $4\times 4\times 4$ nm^3. To approximate an extended plate, periodic boundary conditions were applied in the xy-plane. The FIB-damaged surface layer, 8 nm thick, was modeled as two cuboid layers at the top and bottom surfaces, where $\mathcal{D} = 0$.

All simulations were performed using the Excalibur code[64] and independently reproduced with MuMax[65]. Energy minimization was carried out using the conjugate gradient method, as implemented in Excalibur[59]. Lorentz TEM images were calculated in Excalibur following the approach described in Ref. 59. Consistent with the experimental setup, all simulated Lorentz TEM images were computed for a defocus distance of −1 mm.

Data availability

The raw data underlying Fig. 3b, c, e, f in the main text are available at https://doi.org/10.5281/zenodo.18884551. All other data are available from the corresponding authors upon reasonable request.

References

1. Nagaosa, N. & Tokura, Y. Topological properties and dynamics of magnetic skyrmions. *Nat. Nanotechnol.* **8**, 899–911 (2013).
2. Fert, A., Reyren, N. & Cros, V. Magnetic skyrmions: advances in physics and potential applications. *Nat. Rev. Mater.* **2**, 1–15 (2017).
3. Romming, N., Kubetzka, A., Hanneken, C., von Bergmann, K. & Wiesendanger, R. Field-dependent size and shape of single magnetic skyrmions. *Phys. Rev. Lett.* **114**, 177203 (2015).
4. Muckel, F. et al. Experimental identification of two distinct skyrmion collapse mechanisms. *Nat. Phys.* **17**, 395–402 (2021).
5. Peng, L. et al. Dynamic transition of current-driven single-skyrmion motion in a room-temperature chiral-lattice magnet. *Nat. Commun.* **12**, 6797 (2021).
6. Xia, J., Zhang, X., Liu, X., Zhou, Y. & Ezawa, M. Universal quantum computation based on nanoscale skyrmion helicity qubits in frustrated magnets. *Phys. Rev. Lett.* **130**, 106701 (2023).
7. Zhang, X. et al. Skyrmion-skyrmion and skyrmion-edge repulsions in skyrmion-based racetrack memory. *Sci. Rep.* **5**, 7643 (2015).
8. Li, S. et al. Magnetic skyrmions for unconventional computing. *Mater. Horiz.* **8**, 854–868 (2021).

9. Mühlbauer, S. et al. Skyrmion lattice in a chiral magnet. *Science* **323**, 915–919 (2009).
10. Yu, X. et al. Real-space observation of a two-dimensional skyrmion crystal. *Nature* **465**, 901–904 (2010).
11. Yu, X. et al. Near room-temperature formation of a skyrmion crystal in thin-films of the helimagnet fege. *Nat. Mater.* **10**, 106–109 (2011).
12. Hassan, M. et al. Dipolar skyrmions and antiskyrmions of arbitrary topological charge at room temperature. *Nat. Phys.* **20**, 615–622 (2024).
13. Rózsa, L. et al. Skyrmions with attractive interactions in an ultrathin magnetic film. *Phys. Rev. Lett.* **117**, 157205 (2016).
14. Tokura, Y. & Kanazawa, N. Magnetic skyrmion materials. *Chem. Rev.* **121**, 2857–2897 (2020).
15. Heigl, M. et al. Dipolar-stabilized first and second-order antiskyrmions in ferrimagnetic multilayers. *Nat. Commun.* **12**, 2611 (2021).
16. Yu, X. et al. Spontaneous vortex-antivortex pairs and their topological transitions in a chiral-lattice magnet. *Adv. Mater.* **36**, 2306441 (2024).
17. Ohara, K. et al. Reversible transformation between isolated skyrmions and bimerons. *Nano Lett.* **22**, 8559–8566 (2022).
18. Yang, L. et al. Embedded skyrmion bags in thin films of chiral magnets. *Adv. Mater.* **36**, 2403274 (2024).
19. Kern, L.-M.et al. Controlled formation of skyrmion bags. *Adv. Mater.* **37**, 2501250 (2025).
20. Zheng, F. et al. Hopfion rings in a cubic chiral magnet. *Nature* **623**, 718–723 (2023).
21. Chen, X. et al. Laser-induced nucleation of magnetic hopfions. *Preprint available at Research Square* (2025).
22. Li, L. et al. Electrically writing a magnetic heliknoton in a chiral magnet. *Nat. Mater.* https://doi.org/10.1038/s41563-025-02450-0, 1–6 (2026).
23. Outerelo, E. & Ruiz, J. M. Mapping degree theory. In *Graduate Studies in Mathematics*, Vol. 108 (American Mathematical Society Providence, 2009).
24. Rybakov, F. N. *Topological Excitations in Field Theory Models of Superconductivity and Magnetism*. Ph.D. thesis, KTH Royal Institute of Technology, Stockholm http://urn.kb.se/resolve?urn=urn:nbn:se:kth:diva-301652 (2021).
25. Lin, S.-Z., Saxena, A. & Batista, C. D. Skyrmion fractionalization and merons in chiral magnets with easy-plane anisotropy. *Phys. Rev. B* **91**, 224407 (2015).
26. Kuchkin, V. M. & Kiselev, N. S. Turning a chiral skyrmion inside out. *Phys. Rev. B* **101**, 064408 (2020).
27. Zhang, H., Fan, X. & Wang, W. Magnetic skyrmions embedded in a vortex. *J. Magn. Magn. Mater.* **630**, 173354 (2025).
28. Leonov, A. O. Meron-mediated phase transitions in quasi-two-dimensional chiral magnets with easy-plane anisotropy: successive transformation of the hexagonal skyrmion lattice into the square lattice and into the tilted fm state. *Nanomaterials* **14**, 1524 (2024).
29. Rybakov, F. N., Eriksson, O. & Kiselev, N. S. Topological invariants of vortices, merons, skyrmions, and their combinations in continuous and discrete systems. *Phys. Rev. B* **111**, 134417 (2025).
30. Göbel, B., Mook, A., Henk, J., Mertig, I. & Tretiakov, O. A. Magnetic bimerons as skyrmion analogues in in-plane magnets. *Phys. Rev. B* **99**, 060407 (2019).
31. Zhang, X. et al. Static and dynamic properties of bimerons in a frustrated ferromagnetic monolayer. *Phys. Rev. B* **101**, 144435 (2020).
32. Zhang, X., Zhou, Y., Yu, X. & Mochizuki, M. Bimerons create bimerons: proliferation and aggregation induced by currents and magnetic fields: special collection: condensed matter. *Aggregate* **5**, e590 (2024).
33. Li, X. et al. Bimeron clusters in chiral antiferromagnets. *npj Comput. Mater.* **6**, 169 (2020).
34. Jani, H. et al. Antiferromagnetic half-skyrmions and bimerons at room temperature. *Nature* **590**, 74–79 (2021).
35. Shen, L. et al. Dynamics of ferromagnetic bimerons driven by spin currents and magnetic fields. *Phys. Rev. B* **102**, 104427 (2020).
36. Castro, M. et al. Bimerons as edge states in thin magnetic strips. *Nano Lett.* **25**, 7249–7257 (2025).
37. Castro, M. et al. Skyrmion-bimeron dynamic conversion in magnetic nanotracks. *Phys. Rev. B* **108**, 094436 (2023).
38. Zhang, X. et al. Dynamic transformation between a skyrmion string and a bimeron string in a layered frustrated system. *Phys. Rev. B* **104**, L220406 (2021).
39. Sie, E. J. et al. An ultrafast symmetry switch in a Weyl semimetal. *Nature* **565**, 61–66 (2019).
40. Afanasiev, D. et al. Ultrafast control of magnetic interactions via light-driven phonons. *Nat. Mater.* **20**, 607–611 (2021).
41. Büttner, F. et al. Observation of fluctuation-mediated picosecond nucleation of a topological phase. *Nat. Mater.* **20**, 30–37 (2021).
42. Khela, M. et al. Laser-induced topological spin switching in a 2d van der Waals magnet. *Nat. Commun.* **14**, 1378 (2023).
43. Berruto, G. et al. Laser-induced skyrmion writing and erasing in an ultrafast cryo-lorentz transmission electron microscope. *Phys. Rev. Lett.* **120**, 117201 (2018).
44. Fu, X. et al. Optical manipulation of magnetic vortices visualized in situ by Lorentz electron microscopy. *Sci. Adv.* **4**, eaat3077 (2018).
45. Eggebrecht, T. et al. Light-induced metastable magnetic texture uncovered by in situ Lorentz microscopy. *Phys. Rev. Lett.* **118**, 097203 (2017).
46. Liu, C., Hu, X., Li, Z., Cao, X. & Fu, X. A strategy for fast and precise control of polarity and chirality in magnetic vortices. *Front. Phys.* **20**, 022201 (2025).
47. Tokunaga, Y. et al. A new class of chiral materials hosting magnetic skyrmions beyond room temperature. *Nat. Commun.* **6**, 7638 (2015).
48. Bitla, Y. et al. Chiral-fluctuations mediated helical to paramagnetic phase transition and scaling study in β-mn type Co8Zn8Mn4 chiral magnet. *J. Phys. Condens. Matter* **35**, 175801 (2023).
49. Henderson, M. E. et al. Characterization of a disordered above room temperature skyrmion material Co8zn8mn4. *Materials* **14**, 4689 (2021).
50. Gioia, G. & James, R. D. Micromagnetics of very thin films. *Proc. R. Soc.London Series A* **453**, 213–223 (1997).
51. García-Cervera, C. J. One-dimensional magnetic domain walls. *Eur. J. Appl. Math.* **15**, 451–486 (2004).
52. Di Fratta, G., Muratov, C. B., Rybakov, F. N. & Slastikov, V. V. Variational principles of micromagnetics revisited. *SIAM J. Math. Anal.* **52**, 3580–3599 (2020).
53. Rybakov, F., Borisov, A. & Bogdanov, A. Three-dimensional skyrmion states in thin films of cubic helimagnets. *Phys. Rev. B* **87**, 094424 (2013).
54. Meynell, S., Wilson, M., Fritzsche, H., Bogdanov, A. & Monchesky, T. Surface twist instabilities and skyrmion states in chiral ferromagnets. *Phys. Rev. B* **90**, 014406 (2014).
55. Rybakov, F. N., Borisov, A. B., Blügel, S. & Kiselev, N. S. New spiral state and skyrmion lattice in 3d model of chiral magnets. *New J. Phys.* **18**, 045002 (2016).
56. Je, S.-G. et al. Creation of magnetic skyrmion bubble lattices by ultrafast laser in ultrathin films. *Nano Lett.* **18**, 7362–7371 (2018).
57. Li, Z. et al. Room-temperature sub-100 nm néel-type skyrmions in non-stoichiometric van der waals ferromagnet $Fe_{3-x}GaTe_2$ with ultrafast laser writability. *Nat. Commun.* **15**, 1017 (2024).
58. Rybakov, F. N., Borisov, A. B., Blügel, S. & Kiselev, N. S. New type of stable particlelike states in chiral magnets. *Phys. Rev. Lett.* **115**, 117201 (2015).
59. Zheng, F. et al. Magnetic skyrmion braids. *Nat. Commun.* **12**, 5316 (2021).

60. Leonov, A., Monchesky, T., Loudon, J. & Bogdanov, A. Three-dimensional chiral skyrmions with attractive interparticle interactions. *J. Phys. Condens. Matter* **28**, 35LT01 (2016).
61. Du, H. et al. Interaction of individual skyrmions in a nanostructured cubic chiral magnet. *Phys. Rev. Lett.* **120**, 197203 (2018).
62. Davoli, E., Di Fratta, G., Praetorius, D. & Ruggeri, M. Micromagnetics of thin films in the presence of dzyaloshinskii–moriya interaction. *Math. Models Methods Appl. Sci.* **32**, 911–939 (2022).
63. Zheng, F. et al. Skyrmion–antiskyrmion pair creation and annihilation in a cubic chiral magnet. *Nat. Phys.* **18**, 863–868 (2022).
64. Rybakov, F. N. & Babaev, E. Excalibur software. http://quantumandclassical.com/excalibur/.
65. Vansteenkiste, A. et al. The design and verification of MuMax3. *AIP Adv.* **4**, 107133 (2014).

Acknowledgements

This work was supported by the National Natural Science Foundation of China, Grant Nos. U22A6005 (J.Q.L., J.L., H.X.Y. and H.F.T.) and 12364018 (Z.A.L.); the National Key R & D Program of China, Grant Nos. 2021YFA13011502 (H.X.Y. and J.Q.L.), 2024YFA1611303 (S.S.S. and Y.Z.), 2024YFA1408701 (J.Q.L.) and 2024YFA1408403 (H.X.Y.); the Natural Science Foundation of Guangxi Province, Grant No. 2024GXNSFDA010014 (Z.A.L.); N.S.K. acknowledges the European Research Council under the European Union's Horizon 2020 Research and Innovation Programme (Grant No. 856538 - project "3D MAGiC"). F.N.R. and O.E. acknowledge the Swedish Research Council (Grant No. 2023-04899). O.E. acknowledges eSSENCE, STandUPP and the European Research Council (FASTCORR Project No. 854843), WISE - the Wallenberg Initiative Materials Science, funded by the Knut and Alice Wallenberg Foundation and the Knut and Alice Wallenberg Foundation from the Projects No. KAW 2022.0108 and No. KAW 2022.0252. This work was carried out at the Synergetic Extreme Condition User Facility (SECUF, https://cstr.cn/31123.02.SECUF).

Author contributions

J.Q.L. supervised the project. K.X.Z. and Z.A.L. conceived the idea and designed the experiments. K.X.Z. and Z.W. fabricated the Co-Zn-Mn thin plates. K.X.Z., S.S.S., W.L.G., and W.T.W. performed the TEM experiments. N.S.K., F.N.R. and O.E. developed the theory and performed the numerical simulations. K.X.Z., N.S.K., and Z.A.L. performed the data analysis and drafted the manuscript. All the authors discussed the results, and J.L., H.F.T., H.X.Y., and Y.Z. contributed to the final manuscript.

Competing interests

The authors declare no competing interests.

Additional information

Supplementary information The online version contains supplementary material available at https://doi.org/10.1038/s41467-026-71291-5.

Correspondence and requests for materials should be addressed to Nikolai S. Kiselev, Zian Li or Jianqi Li.

Peer review information *Nature Communications* thanks the anonymous reviewer(s) for their contribution to the peer review of this work. A peer review file is available.